High-temperature nodal ring semimetal in two-dimensional honeycomb-kagome Mn_2N_3 lattice

Xin-Ke Liu(刘鑫柯), Xin-Yang Li(李欣阳), Miao-Juan Ren(任妙娟)†,
Pei-Ji Wang(王培吉), and Chang-Wen Zhang(张昌文)‡

School of Physics and Technology, University of Jinan, Jinan 250022, *China*

(Received 15 July 2022; revised manuscript received 9 September 2022; accepted manuscript online 15 September 2022)

The search for two-dimensional (2D) nodal ring semimetallic materials is a current research hotspot in spintronics, and designing a 2D nodal ring (NR) material with high Curie temperature (T_C) and strong robustness to spin–orbit coupling (SOC) is an even greater challenge. Here, based on the first-principles calculations and symmetry analysis, we predict that 2D Mn_2N_3 is a nodal ring semimetal (NRSM) with three energy bands near the Fermi energy level consisting of electrons in the same spin channel. An electron-like energy band and two hole-like energy bands near the Fermi plane cross to form two NRs centered at the point Γ. Symmetry analysis shows that the spin-polarized NR semimetal is robust to SOC due to the conservation of horizontal mirror symmetry. Monte-Carlo simulations further demonstrate that the T_C of the 2D Mn_2N_3 reaches 530 K, well above the room temperature. Notably, the 2D Mn_2N_3 remains an NRSM on h-BN substrate. Our results not only reveal a general framework for designing 2D NR materials, but also promote further research in the direction of multifunctional quantum devices for spintronics.

Keywords: first-principles calculation, semi-metal, nodal ring, Curie temperature

PACS: 72.25.–b, 31.15.A–, 31.15.ae, 31.15.aj **DOI:** 10.1088/1674-1056/ac921c

1. Introduction

Topological semimetals[1–4] are a recent research hotspot in the condensed matter physics. Many remarkable physical properties of graphene are related to its topological semi-metallic energy band structure, i.e., the conduction and valence bands of graphene intersect linearly at two isolated Fermi points in the Brillouin zone (BZ). The special energy band structure makes low-energy electrons the same as two-dimensional (2D) massless Dirac fermions.[5] The valence and conduction bands of topological semimetals can cross as dots or lines in the Fermi plane to form Dirac/Weyl semimetals[6–10] or nodal line/ring semimetals. Nodal ring semimetals (NRSM) form closed loops in the k-space where the conduction and valence bands cross continuously in the Fermi plane. NRSM[11–21] is firstly proposed in all-carbon Mackay Terrones crystals,[22] antiperovskite Cu_3PdN[23] and other three-dimensional materials. Recently, the 2D NRSMs have received increasing attention, such as Ba_2CdReO_6[24] and Al_3FeSi_2.[25] Among them, the 2D monolayer Cu_2Si[12] is experimentally confirmed to be an NRSM, and its energy band structure is characterized by two parallel rings centered at the Γ point. NRSMs have many special properties, such as nondispersive Landau energy level,[26] high-temperature surface superconductivity,[27] and long-range Coulomb interactions.[28] Symmetry breaking may lead to the transformation of NRSM into other exotic topological states such as topological insulators and Weyl semimetals.[29,30] In general, the formation of ferromagnetic (FM) sequences is accompanied by time-reversal symmetry (TRS) breaking and sometimes by symmetry reduction of the crystal symmetry. Therefore, it is challenging to find NRSM in magnetic materials.

Studying 2D materials which have single-spin properties is notable when the TRS associated with spin is disrupted.[31] A semimetal is a state in which one electron spin channel is in a metallic state and the other electron spin channel is in an insulator or semiconductor. The speed of 100% polarized electrons or holes in a semi-metallic material is much faster than that of unpolarized electrons in a conventional 2D semiconductor, so it has a natural advantage in spin generation, injection and transport. By adjusting the gate voltage and exploiting the Hall effect, we can obtain a high-speed controlled flow of spin electrons, a property that can be used in devices such as field-effect transistors[32] and self-selecting filters.[33] Furthermore, it is possible that the spin-polarized NRSM materials are precursors of quantum anomalous Hall (QAH) phases that do not require magnetic atom doping, which can considerably expand the range of magnetic topology materials.[34–37] Investigating new materials with spin-polarized nodal rings (NR) is very intriguing, which will bring new practical applications in spintronics and condensed matter physics.

The 2D honeycomb-kagome (HK) lattice provides a fertile ground for the study of exotic physical properties, and previous studies have found some FM Dirac semimetals in the HK lattice.[38,39] In this work, our computational analysis

†Corresponding author. E-mail: ss_renmj@ujn.edu.cn
‡Corresponding author. E-mail: ss_zhangchw@ujn.edu.cn

© 2022 Chinese Physical Society and IOP Publishing Ltd

yields that the HK monolayer Mn_2N_3 possesses a fully spin-polarized NR that is strongly robust to spin–orbit coupling (SOC) interactions. The calculation of magnetic anisotropy energy (MAE) indicates that the ground state of the monolayer Mn_2N_3 is out-of-plane (OP). The Curie temperature (T_C) of Mn_2N_3 is 530 K based on the Ising model and Monte-Carlo (MC) simulations. We next explain the origin of NR using wave function symmetry analysis and an effective tight-binding (TB) model constructed by the maximally localized Wannier function (MLWF). Furthermore, Mn_2N_3 can construct h-BN/Mn_2N_3/h-BN heterostructures with h-BN and maintain its NRSM state, and the above conclusions demonstrate that the monolayer Mn_2N_3 is an ideal material for spintronics devices.

2. Computational details

The Vienna *ab initio* simulation package (VASP),[40] based on the spin polarization density generalized functional theory (DFT), calculates all structural and electronic properties. We use Perdew–Burke–Ernzerhof (PBE) in the form of generalized gradient approximation (GGA)[41] to process the exchange–correlation function. Projection-augmented-wave (PAW)[42] potential is used to describe the ion–electron potential. To explain the Mn-3d orbital correlation effect, the structure is optimized by using a spin-dependent GGA plus Hubbard U,[43] with the Hubbard U parameter set to 3.0 eV. We test some U values and they show the qualitatively similar results. The screened Heyd–Scuseria–Ernzerhof Hybrid functional method (HSE06) is used to confirm the precision of the PBE calculation results. An $11\times11\times1$ Monkhorst–Pack k-points grid is used to integrate the BZ.[44] All the structural parameters are completely relaxed until the total energy and the Hellmann–Feynman force on each atom are converged to 10^{-6} eV and 0.01 eV/Å, respectively. In order to avoid interactions induced by periodic images, a vacuum region exceeding 15 Å is executed. Phonon dispersion curves of $3\times3\times1$ supercells are calculated by using phonopy code[45] based on density functional perturbation theory. We use MC simulations and Ising model to calculate the T_C. *Ab initio* molecular dynamics (MD) calculations are calculated for a $5\times5\times1$ supercell with a time step of 1 fs at 300 K temperature for 8 ps. We use D3 Grimme dispersion in the energy minimization process for the sake of finding the most mechanically stable conformation of the van der Waals (vdW) heterostructures.[46] The effective TB Hamiltonian is obtained by using the MLWF package[47,48] for fitting the energy bands.

3. Results and discussion

As seen in Fig. 1(a), each HK monolayer Mn_2N_3 contains two manganese (Mn) atoms and three nitrogen (N) atoms. The Mn atoms in the Mn_2N_3 share an N bridge with neighboring Mn atoms and three N atoms around each Mn atom, forming a HK lattice with D_{6h} point group symmetry. The crystal structure is similar to that of the 2D organic Ta_2S_3 and Nb_2O_3[35] lattices. The relaxation lattice constant of Mn_2N_3 is $a_1 = a_2 = 6.09$ Å. The N–Mn–N bond angle is 120°, and the Mn–Mn distance is $d = 3.52$ Å. To describe the stability of Mn_2N_3 bonding, we calculate the cohesion energy E_c, which is calculated as follows:

$$E_c = E(Mn_2N_3) - 2\mu(Mn) - \frac{3}{2}\mu(N_2), \tag{1}$$

where $E(Mn_2N_3)$ is the energy of the Mn_2N_3 and μ(Mn) and $\mu(N_2)$ are the chemical potentials of Mn atoms and N_2 molecules, respectively. The cohesion energy of the Mn_2N_3 is $E_c = -0.602$ eV/atom, which is comparable to that of the monolayer CrI_3 (−0.903 eV/atom)[49] and $Cr_2Ge_2Te_6$ (−0.552 eV/atom).[50] The large cohesion energy indicates that the synthesis of the Mn_2N_3 is an exothermic chemical reaction with stable bonding within the lattice. To illustrate the bonding properties of the Mn_2N_3, we calculate the electron localization function (ELF) in the (001) and (110) planes. As illustrated in Fig. 1(b), the electrons are mainly localized around the N atom and almost no electrons are located around the Mn atom or in the central region between Mn and N. This indicates that the electrons are transferred from the Mn atom to the N atom, which is a typical ionic bonding property. The ionic bond between Mn and N is related to the large electronegativity difference between the bonding atoms.

The stability of the 2D materials is decisive for their experimental fabrication and deeper applications. In the first place, to demonstrate the kinetic stability of the Mn_2N_3, we calculate the phonon spectrum of the Mn_2N_3, as Fig. 1(d) shows. We can see that there are no imaginary frequencies in the full BZ, which indicates that the monolayer Mn_2N_3 lattice is kinetically stable. In the second place, we use MD simulations to estimate the thermodynamic stability of the Mn_2N_3 lattice. As depicted in Fig. 1(e), the crystal structure of the Mn_2N_3 is not significantly deformed in the MD simulations within 8 ps at 300 K temperature. Last but not least, we calculate the elastic constants of the monolayer Mn_2N_3. The elastic constants can reflect the mechanical stability of the material. By using Voigt notation, the elastic tensor $\boldsymbol{C}$ of a 2D material with D_{6h} point group symmetry can be simplified as

$$\boldsymbol{C} = \begin{pmatrix} C_{11} & C_{12} & 0 \\ C_{12} & C_{11} & 0 \\ 0 & 0 & (C_{11}-C_{12})/2 \end{pmatrix}. \tag{2}$$

It is calculated that C_{11} and C_{12} are equal to 32.47 GPa and 25.22 GPa, respectively. Both C_{11} and $C_{11}-C_{12}$ are greater than 0, which satisfy Born's mechanical stability judgment criteria and confirm the mechanical stability of the monolayer

Mn_2N_3. In conclusion, the above results indicate that the Mn_2N_3 monolayers have very good structural stability and are promising to be prepared in the laboratory.

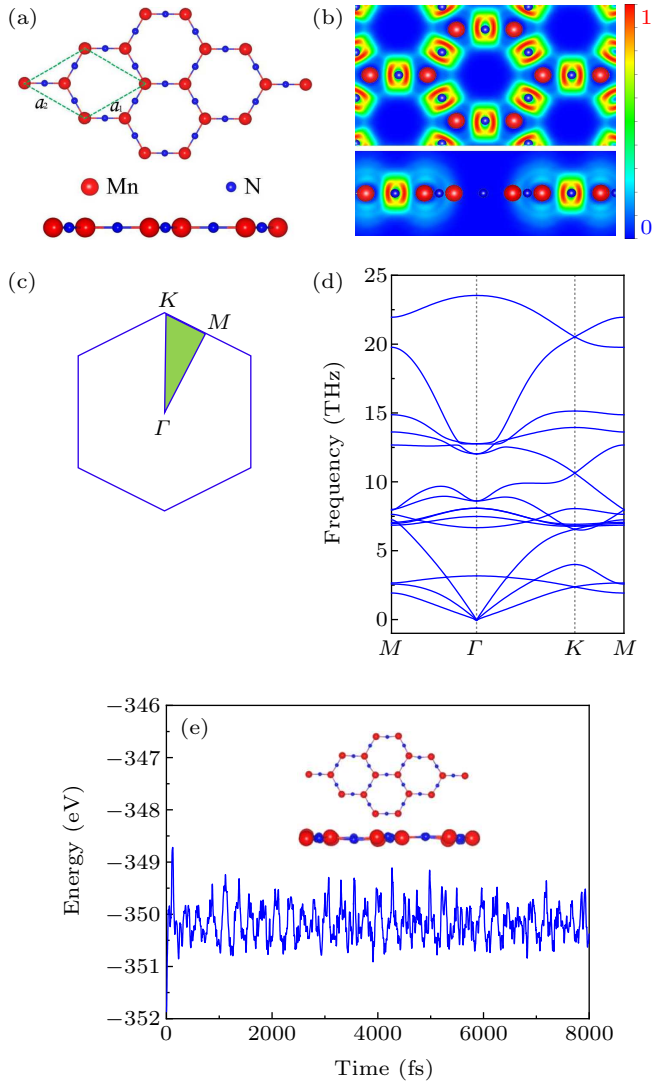


Fig. 1. (a) Top and side views of the monolayer Mn_2N_3 lattice, where the Mn atoms are in red and the N atoms are in blue. (b) ELF maps of the (001) and (100) facets of the Mn_2N_3 lattice, with the charge aggregation distribution represented by normalized color mapping, blue for no charge present and red for charge concentration. (c) 2D BZ representation of the monolayer Mn_2N_3. (d) Phonon spectrum of the monolayer Mn_2N_3. (e) MD simulation at 300 K temperature.

After demonstrating the structural stability of the Mn_2N_3, we next investigate the magnetic properties of the Mn_2N_3. The spin-polarized electronic properties can be illustrated by the differential electron density of the upper and lower spin channels. Spin polarization calculations show a net magnetic moment of $M = 5\mu_B$ per unit cell, indicating a large spin polarization in the Mn_2N_3. The local magnetic moment of the Mn atom is $M_{Mn} = 3.202\mu_B$, which is consistent with the high spin state of Mn^{3+}. The nitrogen atoms have a very small opposite magnetic moment ($M_N = -0.47\mu_B$) due to the fact that they are antiferromagnetically coupled to the Mn atoms and are hardly magnetized. It is also evident from the spin density diagram in Fig. 2(a) that the spin polarization is dominated by the Mn atom. To identify the magnetic ground state of the Mn_2N_3, we design some possible antiferromagnetic configurations, which include Neal antiferromagnetic (NAFM), stripe AFM (SAFM) and zigzag AFM (ZAFM), and FM, as illustrated in Fig. 2(b). The calculated energy of NAFM, SAFM, and ZAFM states is 37.33 meV, 22.49 meV, and 13.47 meV, respectively, higher than that of FM state ($\Delta E = E_{AFM} - E_{FM}$). So the Mn_2N_3 ground state is the FM state. MAE describes the energy required to rotate the magnetization direction of the FM state from the magnetic easy axis to the magnetic hard axis, reflecting the difficulty of spin flip and the magnetic moment orientation in the ground state. We consider the SOC effect in the MAE calculations when calculating the energy for different magnetic moment orientations. MAE calculations show that the magnetic ground state of Mn_2N_3 is in the OP [001] direction.

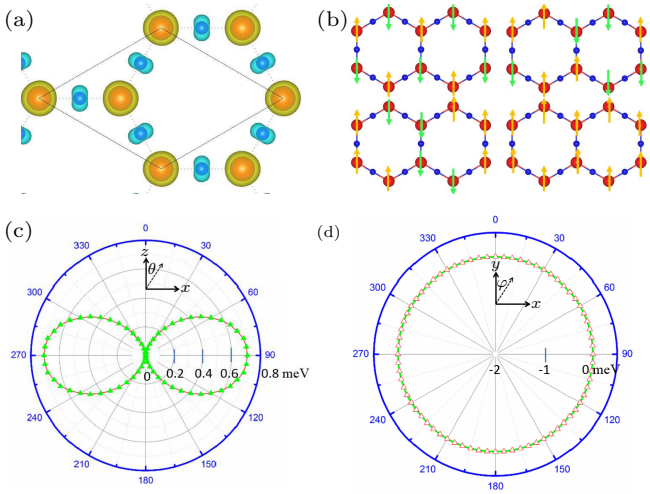


Fig. 2. (a) Spin density map of the (001) plane. (b) Four possible magnetic configurations of the monolayer Mn_2N_3: Upper left NAFM, upper right SAFM, lower left ZAFM, and lower right FM. (c) Difference between the energy of the magnetic moment in each direction from 0° to 360° in the *xz* plane θ and the base state energy. (d) Difference between the energy of the magnetic moment in each direction from 0° to 360° in the *xy* plane φ and the base state energy.

The T_C is another critical parameter for spintronic devices in practical applications. Before applying Mn_2N_3 to spintronic devices, the relationship between the magnetic properties of the Mn_2N_3 and temperature needs to be explored. By using the 2D Ising model to calculate T_C, the spin Hamiltonian can be formulated as

$$H = -\sum_{ij} J_1 S_i S_j - \sum_{ik} J_2 S_i S_j - A S_i^z S_j^z, \tag{3}$$

where J_1 and J_2 are respectively the nearest and second nearest neighbor parameters of the magnetic exchange interaction. S_i is the atomic spin vector. A is the anisotropy parameter, and S^z is the z-component of the spin vector. Because of the larger distance between two second nearest neighbor Mn atoms (J_2 term is neglected) and the smaller MAE energy (A term is neglected), the spin Hamiltonian only considers the J_1 term. The J_1 term can be expressed as $J_1 = \Delta E/(2zS_{TM}^2)$, where

$\Delta E = E_{\rm FM} - E_{\rm AFM}$, z is the number of nearest neighbor magnetic atoms, $S_{\rm TM}$ is the magnitude of the magnetic moment of the magnetic atom. The final value of J_1 is 6.1 meV and $T_{\rm C}$ is 530 K. The red curve in Fig. 3 shows the image of the variation of the single-cell magnetic moment with temperature. The single-cell magnetic moment decreases significantly at $T_{\rm C} = 530$ K which indicates that the maximum temperature at which the FM state can be maintained is 530 K. In addition, we calculate the specific heat capacity ($C_{\rm V}$) using the following equation:

$$C_{\rm V} = \frac{\langle E^2 \rangle - \langle E \rangle^2}{\langle L^2 T^2 \rangle}, \tag{4}$$

where E is the energy of each magnetic configuration. The calculated $C_{\rm V}$ is shown by the green curve in Fig. 3, which further confirms the ferromagnetic–paramagnetic phase transition with critical temperature of 530 K. The high $T_{\rm C}$ indicates that the monolayer Mn_2N_3 is a promising material for high-temperature spintronics.

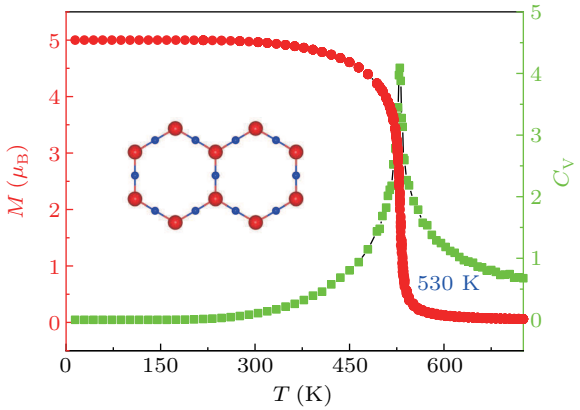


Fig. 3. MC simulation plot with red indicating the magnetic moment magnitude versus temperature curve and green indicating the specific $C_{\rm V}$ versus temperature curve.

We next investigate the electronic properties of the monolayer Mn_2N_3. The first one, in Fig. 4(a), the electronic bands with spin up and spin down are shown in blue and red, respectively. As can be seen, the electrons near the Fermi plane are completely separated from each other, and the spin-down electrons carry a wide band gap of 2.08 eV, whilst the spin-up electron band has no band gap. Consequently, in the vicinity of the Fermi energy level, the electrons are fully spin-polarized. The second one is that we observe a linear crossing of the three energy bands near the Fermi energy level. In these three energy bands, one is an electron-like band (marked as γ band), the other two are hole-like bands (marked as α and β bands), and band crossover occurs between γ band and α, β bands. In the projection of the orbitals in Figs. 4(b) and 4(c), it is observed that the α and β bands are largely attributed to the Mn(d_{xy}, $d_{x^2-y^2}$), N(p_{x+y}) orbitals, whereas the γ band is mostly contributed by the Mn(d_{yz}), N(p_z) orbitals. We further calculate the 3D energy bands and find that these crossings do not appear in isolation. On the contrary, they are part of two concentric rings centered at the point Γ as displayed in Figs. 5(a) and 5(b). In Figs. 5(c) and 5(d), we label the outer and inner rings as L_1 and L_2, respectively. It is worth noting that the L_1 shape is a hexagon around the Γ point. The hexagonal L_1 band crossings are anisotropic, which will bring many interesting phenomena.

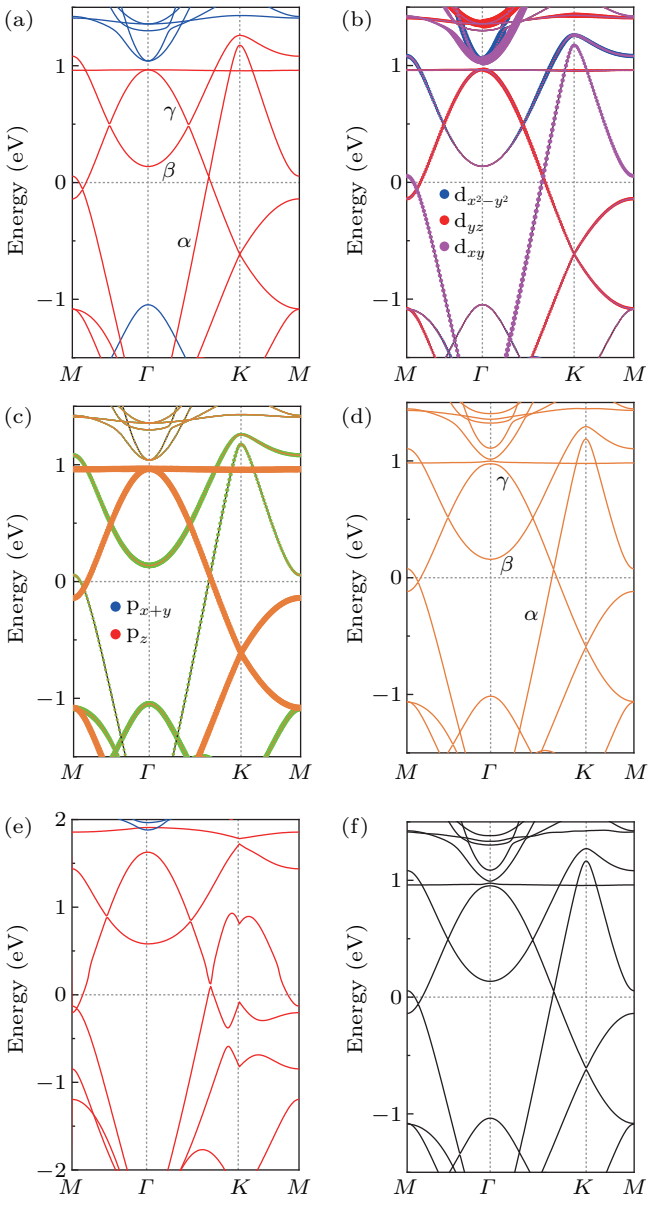


Fig. 4. (a) Electronic energy band diagrams of the upper spin (red) and lower spin (blue) channels of the monolayer Mn_2N_3 without considering SOC. (b) Analytical diagram of the orbital composition of the Mn atom, with the energy bands near the Fermi plane mainly contributed by $d_{x^2-y^2}$, d_{yz}, d_{xy} orbitals. (c) Analytical diagram of the orbital composition of the N atom, the energy bands near the Fermi surface are mainly contributed by p_{x+y}, p_z orbitals. (d) Electron energy band diagram (yellow) of the monolayer Mn_2N_3 with SOC. (e) Band structure calculated by the HSE06 method. (f) TB model fitted energy bands (black lines).

Then we calculate the electronic properties after considering the SOC effect. The yellow line in Fig. 4(d) shows the electronic energy band diagram along the M–Γ–K–M path af-

ter considering the SOC effect. It is worth noting that the energy band along the M–Γ–K–M path under the SOC effect is not opened with a gap. We also examine the other parts of both NR and no band gaps are found to exist. The above results indicate that the NR in the monolayer Mn_2N_3 is stable to SOC. In addition, to verify the accuracy of the PBE calculation results, we calculate the HSE06 energy band using the accurate and reliable HSE06 hybrid function algorithm, as shown in Fig. 4(e). It can be seen from the figure that only L_1 opens a tiny band gap of 10 meV in the Γ–K path, which has little effect on the application of the nodal ring, and the results of the HSE06 and PBE calculations are qualitatively the same.

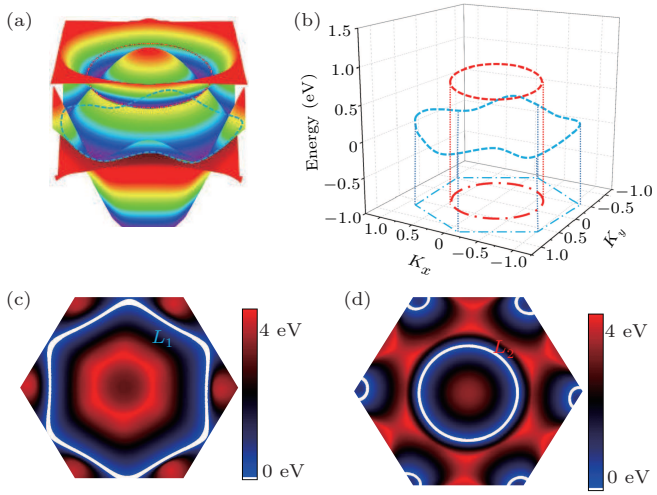


Fig. 5. (a) The monolayer Mn_2N_3 3D energy band. (b) The NR formed by the intersection of α, β, and γ bands, with the outer ring defined as L_1 and the inner ring defined as L_2. (c) Top view of the NR L_1. (d) Top view of the NR L_2.

Then, it is natural to wonder what protects the NR in the monolayer Mn_2N_3. Through analysis of the symmetries for the three bands, we believe that NR is protected by horizontal mirror (M_z) symmetry. The ground-state magnetization direction is perpendicular horizontal facing outward, such that the magnetization direction does not destroy the M_z in the FM state. The M_z eigenvalues of the two hole-like bands α and β are $+$i, while the M_z eigenvalues of the electron-like band γ are $-$i, so the γ band must cross the α and β bands without hybridization. As long as M_z is present, the energy band crossing will not open the band gap even under SOC action, and NR is thus protected. Next, we construct TB model Hamiltonian by projecting the d_{xy}, $d_{x^2-y^2}$, and d_{yz} orbitals of the Mn atoms and p_{x+y} and p_z of the N atoms onto the Mn_2N_3 cell using the MLWF for further analysis of the energy band structure. As indicated in the black line in Fig. 4(f), the main features of the DFT calculated energy band considering SOC and the TB model fitted energy band around the E_f level are the same, despite the subtle differences. Furthermore, because of the M_z symmetry, the eigenstates have to be spin-polarized oriented along the OP, i.e., no hybridization occurs in the spin-up and spin-down energy band, and those energy bands are fully spin-polarized. In summary, the monolayer Mn_2N_3 is a novel material protected by M_z with fully spin-polarized NR under the action of SOC. It is not difficult to infer that when breaking M_z, NRs will also be broken. To verify the above conjecture, we rotate the magnetic moments to $\theta = 45°$ and $\theta = 90°$ directions, respectively, and calculate their energy band diagrams. As presented in Fig. 6, since the M_z symmetry is broken, the energy band crossover is opened and the NRs is destroyed into two pairs of Weyl points.

Finally, since growing thin films on the semiconductor substrates with large band gaps is a common practice for experiments, we explore the feasibility of forming heterostructures with a single layer of the Mn_2N_3 on semiconductor substrates. From the stress–energy band diagram in Fig. 8, it can be seen that the Mn_2N_3 lattice nodal ring property is robust to compressive stresses and maintains the nodal ring energy band characteristics even at 2% tensile stress. We place Mn_2N_3 on the h-BN[51] substrates to form h-BN/Mn_2N_3/h-BN heterostructures, as showed in Fig. 7(a). Structural optimization considering van der Waals corrections shows that the layer spacing between the Mn_2N_3 and the h-BN is 3.0 Å, which is typically of weak vdW interactions. Figure 7(b) shows the electronic energy band structure of the heterostructures. We

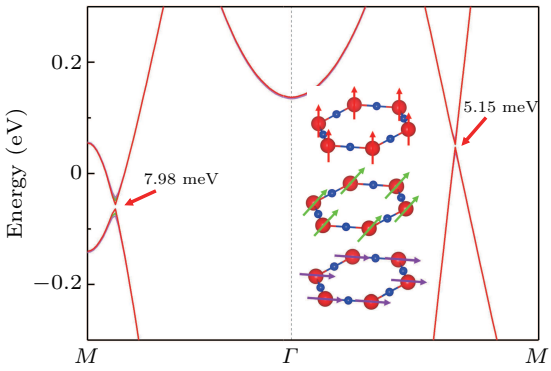


Fig. 6. The energy band diagrams when the direction of the magnetic moment is along $\theta = 0°$, $\theta = 45°$, and $\theta = 90°$ are shown in red, green, and purple, respectively.

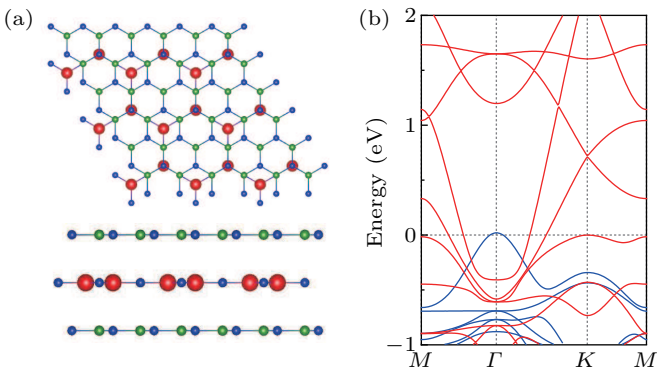


Fig. 7. (a) Top and side views of the h-BN/Mn_2N_3/h-BN heterostructures, where the N atom is directly above the Mn atom. (b) Electron energy band diagram of the heterostructures.

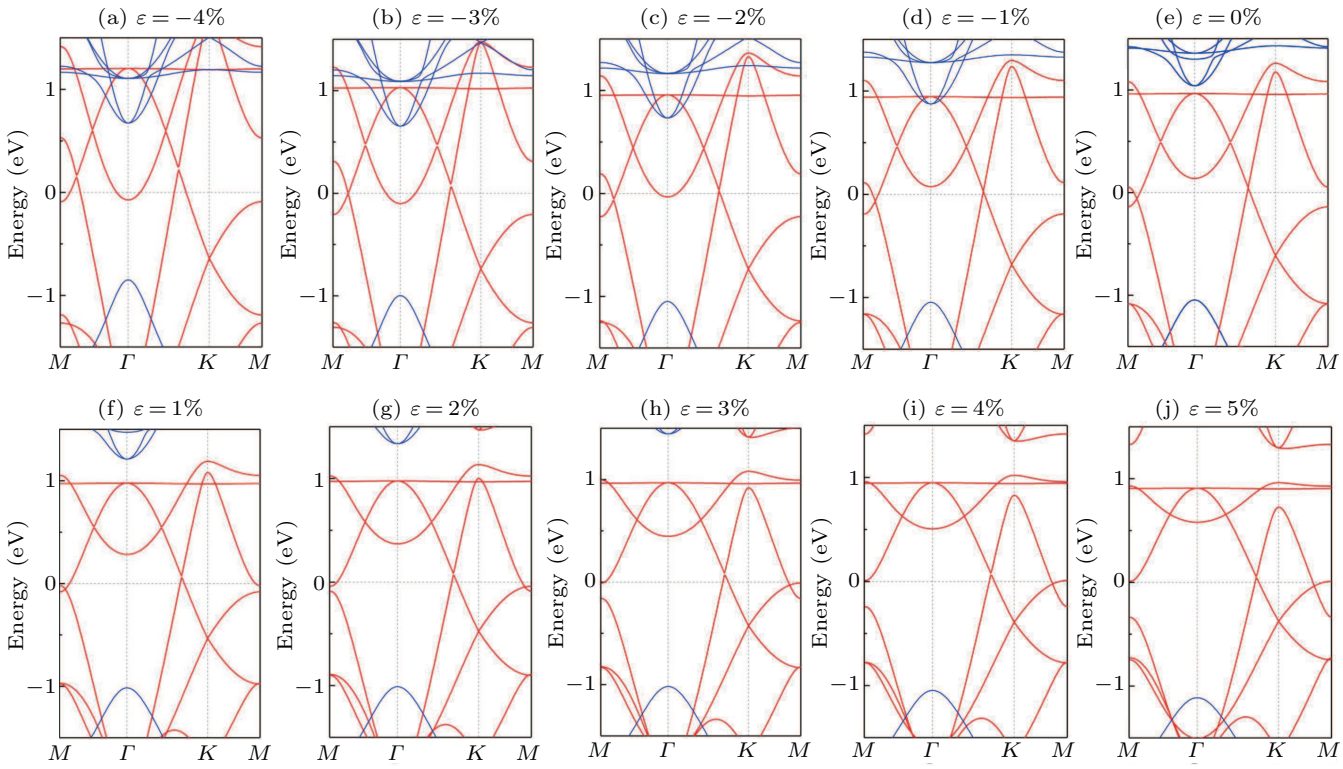


Fig. 8. Band structures of the Mn_2N_3 under different biaxial strain.

can see that the energy band structure and FM properties of the Mn_2N_3 can be well maintained on the h-BN/Mn_2N_3/h-BN heterostructures, and the NR near the E_f level is essentially the same as that of monolayer Mn_2N_3. This is due to the preservation of the M_z mirror symmetry by placing the monolayer Mn_2N_3 between two h-BNs.

4. Conclusion and perspectives

We propose that the 2D monolayer Mn_2N_3 is a FM NRSM, which has thermodynamical and kinetical stability. Based on the Ising model and MC simulations, a T_C of 530 K is obtained, higher than that of most of the found 2D NRSMs. Analysis of the electron energy band structure shows that the electron and hole bands with the same spin component are in linear contact with each other near the E_f to form two NRs centered at the Γ point. There are much faster spin-polarized carriers in the monolayer Mn_2N_3 than that of in the non-spin-polarized materials. Because of the protection of M_z symmetry, NR is robust to SOC. Then we elucidate the origin of NR by symmetry analysis and TB model. Finally, we demonstrate that the monolayer Mn_2N_3 can form h-BN/Mn_2N_3/h-BN heterostructures with h-BN and maintain NR properties. The 2D Mn_2N_3 is a promising candidate for the experimental observation of spin-polarized NR fermions and gives a motivating platform to design new spintronics devices.

Acknowledgments

Project supported by Taishan Scholar Program of Shandong Province, China (Grant No. ts20190939), Independent Cultivation Program of Innovation Team of Jinan City (Grant No. 2021GXRC043), and National Natural Science Foundation of China (Grant Nos. 52173283 and 62071200).

References

[1] Burkov A 2016 *Nat. Mater.* **15** 1145
[2] Velury S and Hughes T L 2022 *Phys. Rev. B* **105** 184105
[3] Weng H, Dai X and Fang Z 2016 *J. Phys.: Condens. Matter* **28** 303001
[4] Feng X, Zhu J, Wu W and Yang S A 2021 *Chin. Phys. B* **30** 107304
[5] Castro Neto A H, Guinea F, Peres N M R, Novoselov K S and Geim A K 2009 *Rev. Mod. Phys.* **81** 109
[6] Chen Y, Xie Y, Yang S A, Pan H, Zhang F, Cohen M L and Zhang S 2015 *Nano Lett.* **15** 6974
[7] Steinberg J A, Young S M, Zaheer S, Kane C L, Mele E J and Rappe A M 2014 *Phys. Rev. Lett.* **112** 036403
[8] Liu Z, Zhou B, Zhang Y, Wang Z, Weng H M, Prabhakaran D, Mo S K, Shen Z, Fang Z and Dai X 2014 *Science* **343** 864
[9] Wieder B J, Kim Y, Rappe A and Kane C 2016 *Phys. Rev. Lett.* **116** 186402
[10] Watanabe H, Po H C, Zaletel M P and Vishwanath A 2016 *Phys. Rev. Lett.* **117** 096404
[11] Li S, Liu Y, Wang S S, Yu Z M, Guan S, Sheng X L, Yao Y and Yang S A 2018 *Phys. Rev. B* **97** 045131
[12] Feng B, Fu B, Kasamatsu S, Ito S, Cheng P, Liu C C, Feng Y, Wu S, Mahatha S K and Sheverdyaeva P 2017 *Nat. Commun.* **8** 1
[13] Chen C, Zeng X T, Chen Z, Zhao Y, Sheng X L and Yang S A 2022 *Phys. Rev. Lett.* **128** 026405
[14] Du X L, Chen R, Wang R and Xu D H 2022 *Phys. Rev. B* **105** L081102
[15] Jin L, Zhang X, Liu Y, Dai X and Liu G 2022 *Phys. Rev. B* **105** 075414
[16] Li X Y, Zhang M H, Ren M J and Zhang C W 2020 *Phys. Chem. Chem. Phys.* **22** 27024
[17] Pang Z X, Zhao Y C, Ji W X, Wang Y and Li P 2021 *Phys. Chem. Chem. Phys.* **23** 12280

[18] Li K K and Hu J P 2017 *Chin. Phys. Lett.* **34** 077501
[19] Fang C, Weng H, Dai X and Fang Z 2016 *Chin. Phys. B* **25** 117106
[20] Chen S, Lou Z, Zhou Y, Chen Q, Xu B, Wu C, Du J, Yang J, Wang H and Fang M 2021 *Chin. Phys. Lett.* **38** 017202
[21] Li J, Zhao L X, Wang Y Y, Wang X M, Ma C Y, Zhu W L, Gao M R, Zhang S, Ren Z A and Chen G F 2019 *Chin. Phys. B* **28** 046202
[22] Weng H, Liang Y, Xu Q, Yu R, Fang Z, Dai X and Kawazoe Y 2015 *Phys. Rev. B* **92** 045108
[23] Yu R, Weng H, Fang Z, Dai X and Hu X 2015 *Phys. Rev. Lett.* **115** 036807
[24] Zhao X, Guo P J, Ma F and Lu Z Y 2021 *Phys. Rev. B* **103** 085138
[25] Takahashi R, Hirayama M and Murakami S 2017 *Phys. Rev. B* **96** 155206
[26] Rhim J W and Kim Y B 2015 *Phys. Rev. B* **92** 045126
[27] Kopnin N, Heikkilä T and Volovik G 2011 *Phys. Rev. B* **83** 220503
[28] Huh Y, Moon E G and Kim Y B 2016 *Phys. Rev. B* **93** 035138
[29] Yan B and Felser C 2016 arXiv: 1611.04182
[30] Soluyanov A A, Gresch D, Wang Z, Wu Q, Troyer M, Dai X and Bernevig B A 2015 *Nature* **527** 495
[31] Ventra M D, Pantelides S and Lang N 2000 *Phys. Rev. Lett.* **84** 979
[32] Li L, Yu Y, Ye G J, Ge Q, Ou X, Wu H, Feng D, Chen X H and Zhang Y 2014 *Nat. Nanotechnol.* **9** 372
[33] Leenheer J, Van Heerde H J, Bijmolt T H and Smidts A 2007 *Int. J. Res. Mark.* **24** 31
[34] Wu J, Liu J and Liu X J 2014 *Phys. Rev. Lett.* **113** 136403
[35] Zhang S J, Zhang C W, Zhang S F, Ji W X, Li P, Wang P J, Li S S and Yan S S 2017 *Phys. Rev. B* **96** 205433
[36] Qiao Z, Ren W, Chen H, Bellaiche L, Zhang Z, MacDonald A and Niu Q 2014 *Phys. Rev. Lett.* **112** 116404
[37] Wang Y P, Li S S, Zhang C W, Zhang S F, Ji W X, Li P and Wang P J 2018 *J. Mater. Chem. C* **6** 10284
[38] Zhang L, Zhang C W, Zhang S F, Ji W X, Li P and Wang P J 2019 *Nanoscale* **11** 5666
[39] Zhang L, Zhang S F, Ji W X, Zhang C W, Li P, Wang P J, Li S S and Yan S S 2018 *Nanoscale* **10** 20748
[40] Hafner J 2008 *J. Comput. Chem.* **29** 2044
[41] Perdew J P, Burke K and Ernzerhof M 1996 *Phys. Rev. Lett.* **77** 3865
[42] Blöchl P E 1994 *Phys. Rev. B* **50** 17953
[43] Dudarev S L, Botton G A, Savrasov S Y, Humphreys C J and Sutton A P 1998 *Phys. Rev. B* **57** 1505
[44] Monkhorst H J and Pack J D 1976 *Phys. Rev. B* **13** 5188
[45] Togo A and Tanaka I 2015 *Scripta Mater.* **108** 1
[46] Grimme S, Antony J, Ehrlich S and Krieg H 2010 *J. Chem. Phys.* **132** 154104
[47] Mostofi A A, Yates J R, Lee Y S, Souza I, Vanderbilt D and Marzari N 2008 *Comput. Phys. Commun.* **178** 685
[48] Wang X, Yates J R, Souza I and Vanderbilt D 2006 *Phys. Rev. B* **74** 195118
[49] Huang B, Clark G, Navarro-Moratalla E, Klein D R, Cheng R, Seyler K L, Zhong D, Schmidgall E, McGuire M A and Cobden D H 2017 *Nature* **546** 270
[50] Gong C, Li L, Li Z, Ji H, Stern A, Xia Y, Cao T, Bao W, Wang C and Wang Y 2017 *Nature* **546** 265
[51] Liu L, Feng Y and Shen Z 2003 *Phys. Rev. B* **68** 104102